

Investigation of Microstructure and Dry Sliding Wear of Hardfaced Layers Produced by FCAW Using Cored Wire Fe-B-C-Ti Alloy

M. Tavakoli Shoushtari¹, M. Goodarzi^{1*} and H. Sabet²

*mgoodarzi@iust.ac.ir

Received: April 2018 Accepted: August 2018

¹ School of Metallurgy and Materials Engineering, Iran University of Science and Technology, Tehran, Iran.

² Department of Materials Engineering, Karaj Branch, Islamic Azad University, Karaj, Iran.

DOI: 10.22068/ijmse.15.4.19

Abstract: In this study, the microstructure, hardness, and dry sliding wear behavior of the hardfaced layers made by a cored wire Fe-B-C-Ti alloy were investigated. St37 steel was used as the substrate and the deposition of the hardfaced layers was conducted by the flux cored arc welding (FCAW) process under single-, two-, and three-pass conditions. Dry sliding wear tests were performed by a pin-on-disk apparatus, based on ASTM-G99, at room temperature (25°C) at the normal applied loads of 50, 100, and 150 N with a constant speed of 0.08 m/s for a sliding distance of 1000 m. The microstructural and phase analyses were carried out by field emission scanning electron microscopy (FE-SEM) and X-ray diffraction (XRD), respectively. The results showed that the hardfaced layer produced by the single-pass process contains TiC rectangular phase distributed within a matrix containing ferrite and the eutectic of (α -Fe₂B). But, the hardfaced layers produced by the two- and three-pass process contain TiB₂ hexagonal phase in addition to TiC, which prevents the formation of detrimental FeB phase around Fe₂B and reduces the number of micro-cracks. Moreover, the sample hardfaced by the three-pass process had the best wear resistance due to the greater hardness resulted from the higher amounts of TiC and TiB₂ phases. In addition, increasing the number of passes has led to the reduction of wear rate at all the three applied loads. At the applied load of 100 N, the wear mechanism for the all three hardfaced samples was an oxidation wear. However, at the applied load of 150 N, the wear mechanism was a combination of oxidation and delamination.

Keywords: Hardfacing, FCAW, Fe-B-C-Ti, Sliding wear, TiB₂, TiC.

1. INTRODUCTION

Wear is one of the most important causes for the destruction and failure of the engineering components in the related industries leading to the considerable economic losses [1-3]. Producing a wear-resistant layer on the surface of the engineering components is one of the ways to control wear [4-8]. The deposition of hardfaced layer with the aim of achieving the desired thickness and metallurgical bond between the layer and the substrate can be performed by different methods of surface modification, such as arc welding [9, 10], laser, plasma spray [12] and thermal spray [13]. Under impact and abrasive wear condition, the layers deposited by arc welding are preferred because it is a cost-effective method and produces relatively thicker and more resistant layers [14-17]. Flux cored arc welding (FCAW), among other arc welding methods, is an economical process due

to applying a high deposition rate and good efficiency. And, because of its automation ability, it can be used for coating different materials in mass scales [18]. The alloys used for depositing hardfaced layers on carbon and low-alloy steels are divided into two groups: ferrous alloys and non-ferrous alloys. Nowadays, ferrous alloys have attracted more attention from researchers and craftsmen because of their reasonable price and a higher wear resistance compared to non-ferrous alloys [19]. Crushers and excavators work under severe wear conditions and are required to be repaired in a very short time. This is why the hardfacing of their components is carried out by high amounts of ferrous-based hardfacing alloys which has the least time and cost [17-19]. Fe-B-C alloy is a new wear-resistant hardfacing alloy which has drawn great attention in recent years [20, 21]. The boron solubility in iron is very low (its maximum solubility in γ -iron and α -iron is 0.02wt% and 0.0081, respectively). Therefore,

its excessive amount forms a continuous network of eutectic borides (FeB and Fe_2B) increasing the hardness and wear resistance [22, 23]. Since the specific volume and the thermal expansion coefficient of FeB and Fe_2B differ significantly, cracks are nucleated at their interface [24, 25]. Due to the presence of the weak B-B bond in the preferred direction of [002] in Fe_2B lattice, Fe_2B is considered a hard phase with intrinsic brittleness. However, regarding the fact that the boron-rich FeB phase is more brittle than Fe_2B , in industrial applications, there is a more tendency towards the formation of Fe_2B as a strengthening phase [26, 27]. On the other hand, the high brittleness of the columnar Fe_2B phase along grain boundaries leads to the surface delamination and fracture during sliding abrasive wear which in turn reduces the wear resistance [28]. Therefore, in the recent years, improving the toughness of the microstructure obtained by hardfacing using Fe-B-C through controlling the Fe_2B brittleness by adding alloying elements, have been the focus of researchers [28-30]. Dawei Yi *et al.* [29, 31] have reported that adding cerium (Ce) and aluminum (Al) to Fe-B alloy modifies the borides and austenite structures during solidification and increases the wear resistance. Huang *et al.* [32] have improved the hardness and fracture toughness of Fe_2B by adding tungsten (W). A large number of studies have been conducted on the addition of chromium (Cr) to Fe-B-C alloy. The results showed that the morphology of borides is changed and their fracture toughness is improved. Jian *et al.* [26] have indicated that the addition of Cr and manganese (Mn) improves the fracture toughness of M_2B in Fe-B alloy which has a positive effect on increasing the abrasive wear resistance.

In the present study, titanium was chosen as the additive to Fe-B-C alloy due to its mechanical strength, making it a suitable strengthening element in hardfacing alloys. Moreover, the boride produced by Ti is stronger than that produced by iron [33]. Thus, before α -iron and Fe_2B are solidified, the stable and high-melting-point TiB_2 is formed [34]. Ti is also a strong carbidizing element leading to the formation of hard TiC in the presence of carbon, reducing the carbon concentration in the matrix of hardfacing

alloy [35]. In this study, the hardfaced layers were produced by self-shielded FCAW using a cored wire Fe-B-C-Ti alloy under single-, two-, and three-pass conditions. The effect of Ti and B content on the microstructure, hardness and sliding wear behavior of the hardfaced layers was investigated.

2. EXPERIMENTAL PROCEDURE

Three St 37 plain carbon steel plates with dimensions of $200 \times 200 \times 10 \text{ mm}^3$ were chosen as the substrate. Prior to hardfacing, top surfaces of the St37 steel plates were cleaned with acetone to remove all surface contaminations, and then preheated to 150°C . Hardfacing was performed by self-shielded Flux-cored arc welding according to the parameters present in Table 1. It should be noted that welding parameters were determined under standards of ASME Section IX, parts of Qw400 & Qw216. Also, the mentioned welding process was performed as given in Table 1 on 3 series of samples according to Table 2. Classifying of samples was occurred on basis of cored wires and pass numbers; the three samples were welded by Fe-B-C-Ti cored wire during three stage process of single pass, two-pass and three-pass. Subsequently, after the prepared hardfacing coatings was air-cooled to ambient temperature, the plates were cut out to organize different test specimens. Welded samples were labeled according to the pass numbers, respectively given in Table 2. Fig. 1 illustrates the schematic of deposited layers on the substrate in the welding different passes along with the samples prepared for microstructural, hardness and wear studies. Chemical analysis of the base metal and hardfacing layers was obtained by spark emission quantometry measurement using an Oxford Instrument machine. Moreover, according to ASTM D4951-14, boron amount was measured by Induction Coupled Plasma - atomic emission spectrometry test (ICP - AES). The plates were cut to prepare different disk-shape specimens for wear tests, and cubic specimens for microstructural and hardness investigations. The cross sections of cubic

Table1. Welding parameters used in hardfacing process

Process	Cored powder	Polarity	Welding velocity (mm/min)	Heat input (kJ/mm)
FCAW-Self Shield	Ferroboron + Ferrotitanium + iron powder	DCEP	300-330	1.62-1.92
Feeding velocity (m/min)	Cored wire diameter (mm)	Arc length (mm)	Voltage (V)	Current (A)
5-7	3.2	4-5	28-30	330-350

Table2. Labeled samples based on welding wire and pass number

Pass number	Cored wire	Label of sample
single pass	Fe-B-C-Ti	Fe-B-C-Ti-1
two-pass	Fe-B-C-Ti	Fe-B-C-Ti-2
three pass	Fe-B-C-Ti	Fe-B-C-Ti-3

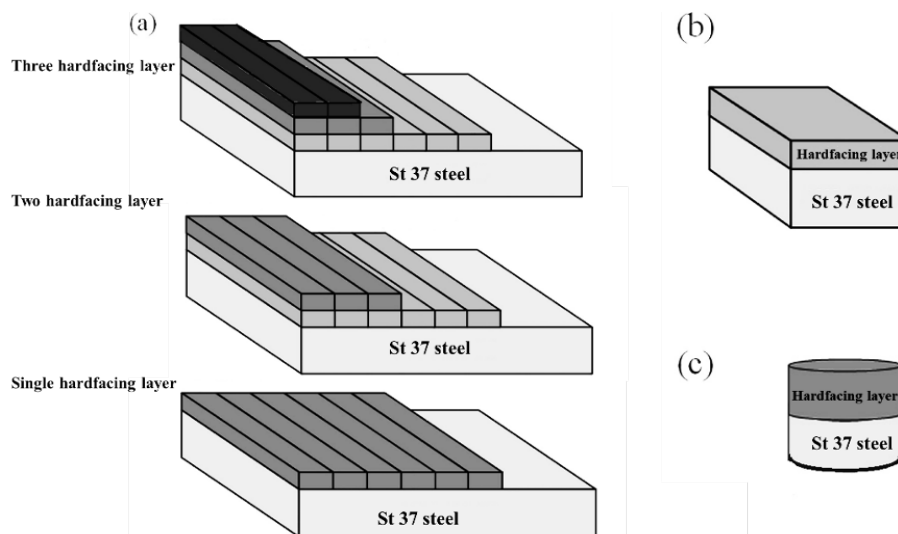


Fig. 1. Schematic illustration of (a) deposited hardfacing layers in different conditions of the welding passes, (b) sample prepared for microstructural and hardness evaluations, and (c) disk specimen prepared for wear test.

specimens were mechanically finished with 2500 mesh SiC papers and finally polished with a cloth using by 1 micron diamond paste. To identify the microstructure constituents in weldment, the cross-section of the hardfacing samples was placed in etching's reagent of an aqueous solution of 10 mL HNO₃ +10mL HCl +10 mL Acetic acid.

Microstructural examinations was studied by a TESCAN MIRA 3 Field Emission – scanning electron microscope (FE-SEM) equipped with an energy dispersive X-ray spectrometer (EDS). For the best contrast between the different hard phases, the secondary as well as the backscattered electrons were detected. A computer-assisted Buhler Omnimet image analysis system was

used to measure the morphological parameters of phases including the length and the volume fraction of particles. X-ray diffraction (XRD) of hardfacing coatings were carried out on grinded top surface of hardfaced layers using Philips X Pert-MPD system with Cu K_α radiation and 40 kV and 30 mA operating conditions and scanning angles between 20° and 90°. Moreover, a BUEHLER hardness tester equipped with Vickers pyramid indenter was utilized for microhardness measurements along the length of cross-section of the specimens. A 100 g load was applied on the indenter for 10 s. It should be noted that each of samples was measured at least three times to increase accurate of macrohardness test results; average amount of these results were considered

as criterion of surface hardness. Dry sliding wear experiments were performed using a pin on-disk machine against the counterface of a ground ($R_a=0.5 \mu\text{m}$) tungsten carbide (WC) pin (diameter 5mm and 15mm length). The WC pin was prepared in the flat contact region by polishing up to $0.5 \mu\text{m}$ (R_a) and cleaning with acetone to remove dust and grease from the surface. In the disk samples (30mm diameter and 10 mm thickness) the hardfaced surface zone was prepared as the contact region of disks. The tests were done in air atmosphere at a relative humidity of $40\pm 2\%$ at room temperature ($25 \text{ }^\circ\text{C}$). Dry sliding were conducted at the applied normal loads of 50, 100 and 150 N, at a constant sliding speed of 0.08 ms^{-1} for a sliding distance of 1000 m. Each test was repeated three times with identical new samples on fresh pin surface and the weight loss determined as a function of distance was used for the analysis of the wear rate. The coefficients of friction for all samples were continuously recorded. Microstructures of worn surfaces and debris collected from the worn disks were investigated using a TESCAN VEGA2 scanning electron microscope (SEM) equipped with the EDS system.

3. RESULTS AND DISCUSSION

3.1. Chemical Composition

The chemical composition of the base metal and the hardfaced layers deposited by different number of passes is given in Table 3.

As can be seen, the chemical composition of the layers varies with respect to the level of base metal dilution during hardfacing process. The amount of B and Ti plays an important role in the hardness and wear resistant of the hardfaced layers. As the number of passes increases, the chemical composition of each layer changes. According to Fe-B phase diagram, given in Fig. 2, with increasing the number of passes, the boron

content in the weld zone increases and lies within the hypereutectic range. The amount of titanium in the weld zone also increases which is due to the higher volume of welding cored wire present in the weld pool. Accordingly, compared to the samples hardfaced by the two- and three-pass process, the sample hardfaced by the single-pass process (coded as Fe-B-C-Ti-1) contains the least amount of B and Ti due to high dilution. It can be found that with increasing the number of passes, the amount of B and Ti has increased by an average of 0.6.

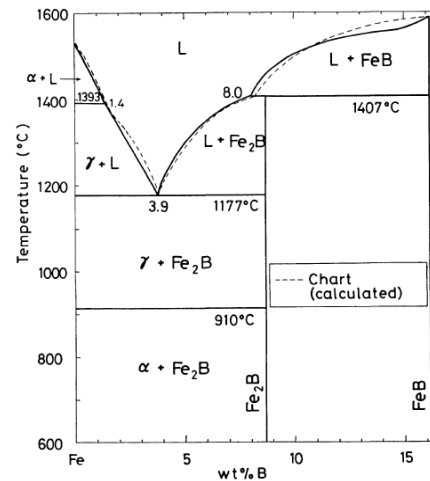


Fig. 2. Fe-B phase diagram [20]

3.2. Microstructure Evaluation

Fig. 3 shows the FE-SEM micrograph of microstructures in SE and BSE contrast. As it is evident, the single-pass deposition has led to the formation of skeletal (columnar) ferritic dendrites and $\alpha\text{-Fe}_2\text{B}$ eutectic dendrites according to the Fe-B phase diagram in Fig. 2 and Fe-C phase diagram. The presence of layered ferritic dendrites can be explained according to the diagram shown in Fig. 2. During the solidification process, based on the amount of boron in the alloy, the solidification line

Table.3. Chemical composition of the substrate and hardfacing layers (in Wt. %).

Sample	C	Si	Mn	B	Ti	Fe
Base metal	0.15	0.15	0.18	-	-	Bal.
Fe-B-C-Ti-1	0.16	0.17	0.21	3.1	1	Bal.
Fe-B-C-Ti-2	0.18	0.19	0.25	3.8	1.6	Bal.
Fe-B-C-Ti-3	0.24	0.23	0.25	4.3	2.4	Bal.

first passes through alpha (α) region and leads to the formation of pre-eutectic ferrite. As the solidification process continues and reaches the eutectic line, the melt composition changes to α -Fe₂B eutectic and the successive layers of α and Fe₂B emerge in the microstructure. Since the cored wire contained Ti and B, backscatter (BSE) imaging mode was used which revealed two polygonal phases with bright and dark color, shown in Fig. 3. Fig. 3(b, d, and f) is the FE-SEM image of these phases at higher magnification. The EDS analysis of the dark particle (1) and the bright particle (2), given in Table 4, confirms the presence of a titanium- and boron-bearing phase. According to the XRD results, shown in Fig. 4, it can be concluded that the rectangular phase and bright irregular polygonal phase are, respectively, TiB₂ and Fe₂B in Fig. 3a. The EDS and XRD analyses, shown in Fig. 3 and Fig. 4, confirm the presence of α and Fe₂B. Fig. 3(c, d) shows the FE-SEM image taken from the surface

of Fe-B-C-Ti-2. As seen, compared to the single-pass process, the two-pass deposition has led to the formation of a relatively different microstructure, consisting of primary Fe₂B phase, ferritic dendrites, and α -Fe₂B eutectic according to the Fe-B phase diagram in Fig. 2 and Fe-C phase diagram. Fig. 3c and Fig. 3d show the images taken in secondary electron (SE) and BSE imaging mode, respectively. Three phases with different shapes are observed, namely bright columnar, dark rectangular, and dark hexagonal. The EDS analyses of the dark particles (3, 5), shown in Table 4, indicate the presence of a titanium-bearing phase. The EDS analysis of the bright particle (4), shown in Table 4, indicates the presence of a boron-bearing phase. According to the XRD results, shown in Fig. 4, it can be concluded that the dark rectangular phase, the dark hexagonal phase, and the long wide columnar phase are, respectively, TiC, TiB₂, and Fe₂B in Fig. 3 c,d. The comparison of the images taken from single-

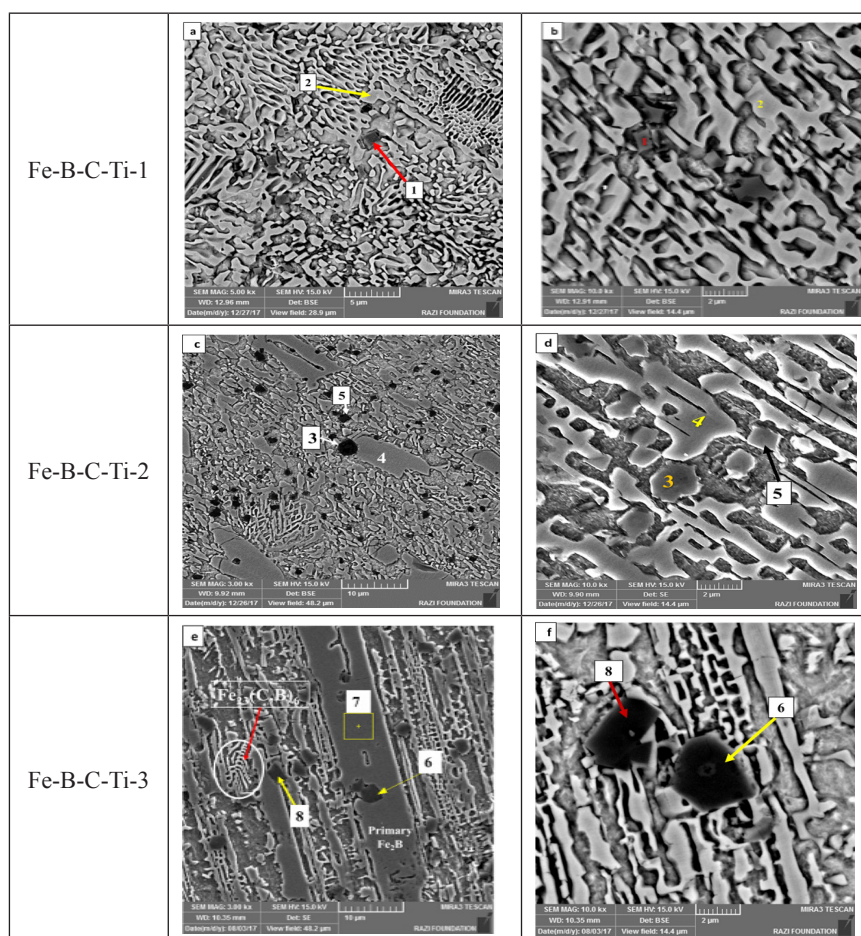


Fig. 3. FE-SEM micrograph of microstructures in SE and BSE contrast.

Table 4. EDS results of different phases in the microstructures of samples shown in Fig.3 (in wt. %).

Phase no.	1	2	3	4	5	6	7	8
Element								
B	14.67	23.50	24.28	25.54	14.15	40.68	30.88	14.62
C	38.27	33.01	17.61	15.14	32.21	10.87	6.24	31.16
Ti	39.59	0.34	39.88	0.21	38.19	39.86	0.26	31.39
Fe	7.47	43.15	15.49	59.11	15.45	3.57	62.51	22.83

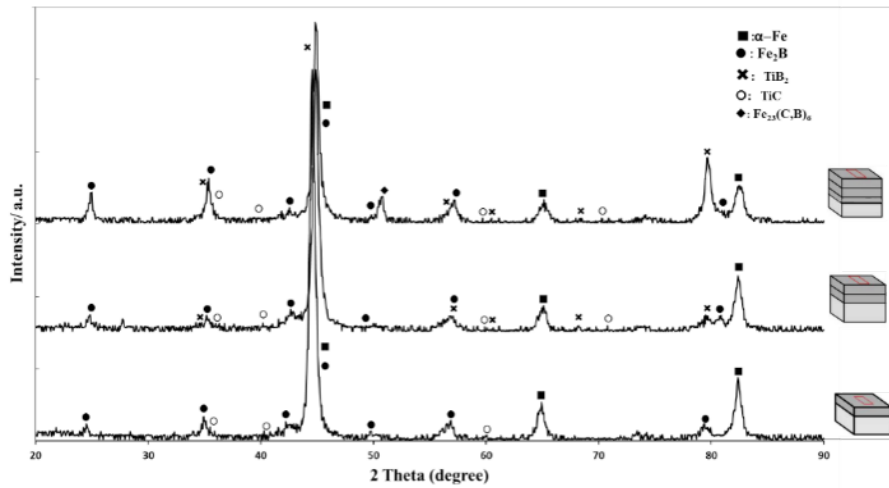


Fig. 4. XRD patterns of the different hardfacing samples.

and two-pass process shows that the latter contains less layered ferritic dendrites than the former and the ferrites have converted to the vermicular shape [36]. However, in the two-pass process, as the boron content is higher, the amount of α - Fe_2B is higher. The volume fraction (%) and average maximum size (μm) of Ti-rich phases shown in Tabel 5, indicate the size of TiC rectangular particles in Fe-B-C-Ti-1 is $1 \times 0.7 \mu m$. The size of these particles in Fe-B-C-Ti-2 is larger and the largest particle is $1.47 \times 1.17 \mu m$. The volume percent of the titanium-bearing phases (TiC) in Fe-B-C-Ti-1 is 17.61 which has increased to 24.46 in Fe-B-C-Ti-2 (TiC+TiB₂). Moreover, by comparing Figs. 3b and 3d, it can be concluded that Fe_2B phase has become larger, longer and wider, and the detrimental FeB phase and cracks are not observed around Fe_2B and the preferred growth location is around the long Fe_2B phase which can explain why no detrimental FeB phase has formed around Fe_2B .

Fig. 3(e, f) shows the FE-SEM image taken from the surface of Fe-B-C-Ti-3. As seen, compared to the other two processes, the third-pass

deposition has led to the formation of a relatively different microstructure containing primary Fe_2B phase in between the vermicular ferritic dendrites and α - $Fe_{23}(C, B)_6$ eutectic. The Fe_2B morphology has changed from the irregular polygon in the second pass to the long rectangle in the third pass in Fig. 3e. The EDS and XRD analyses, shown in Table 4 and Fig. 4, confirm the presence of α and Fe_2B . The comparison of the images taken from the two- and three-pass process shows that the latter contains less layered ferritic dendrites than the former and the ferrites have converted to the vermicular shape. However, in the three-pass process, as the boron content is higher, the amount of α - $Fe_{23}(C, B)_6$ is higher. Moreover, due to the non-equilibrium solidification and the presence of high boron content, at first, the primary Fe_2B is formed. As the solidification continues, α - Fe_2B eutectic is formed along with the primary Fe_2B . The size of TiC rectangular particles in Fe-B-C-Ti-3 is larger and the largest particle is $1.62 \times 3.38 \mu m$ in Table 5. The volume percent of the titanium-bearing phases (TiC+TiB₂) in Fe-B-

C-Ti-3 is 29.58. Moreover, the Fe_2B phase has become longer, and narrower. According to Fig. 3 and XRD analysis in Fig. 4, no detrimental FeB phase and cracks have formed around Fe_2B .

3.3. Microhardness Measurement and Wear Behavior

Fig. 5, shows the average microhardness measurements of the hardfaced samples. As seen, the hardness values of the hardfaced samples varies from 1054 Vickers for the single-pass process to 1245 Vickers for the three-pass process. The higher hardness of Fe-B-C-Ti-3 is related to the higher levels of B and Ti, which has increased the amount of primary Fe_2B , TiC, and TiB_2 in the microstructure. The hardness value of Fe-B-C-Ti-2 has decreased to 1136 Vickers because of the lower amount of Fe_2B , TiC, and TiB_2 . The average hardness value for Fe-B-C-Ti-1 is 1054 Vickers which is the least value. This sample contains less boron and titanium and has a hypoeutectic microstructure. TiB_2 is absent in this sample. Because the Gibbs free energy of formation of TiC is lower than that of TiB_2 and the carbon permeability is greater than boron, carbon easily reacts with Ti and TiC forms sooner [37]. On the other hand, the amount of Ti in Fe-B-C-Ti-1 is low, thereby carbon consumes all the Ti and no TiB_2 is formed. Fig. 6 shows the weight loss variations of the hardfaced samples against the sliding distance at the applied loads of 50, 100, and 150 N. As seen, for all the samples, as the sliding distance increases, the amount of wear increases. Moreover, with increasing the applied load from 50 to 150 N, the weight loss of all the three samples has increased. As seen in Figs. 6a and c, at 150 N, there exists a sudden increase in the weight loss between 500 m and 1000 m. This sudden increase for Fe-B-C-Ti-2 in Fig. 6b, under the same load, is between 750 m and 1000 m. Fig. 7 shows the mean friction coefficient variation for Fe-B-C-Ti-1, Fe-B-C-Ti-2, and Fe-B-C-Ti-3 at 50, 100, and 150 N. As seen, at all loads, Fe-B-C-Ti-3 and Fe-B-C-Ti-1 have the lowest and the highest friction coefficient, respectively. Moreover, for a given sample, the friction coefficient increases with increasing the load. The column graph, given in Fig. 8, show the simultaneous effect of the load and the numbers of passes on the wear rate of Fe-B-C-Ti-1, Fe-B-C-Ti-2, and Fe-B-C-Ti-3 at 100 and 150

N. As seen from Fig. 8 for all the three samples, the wear rate increases with increasing the load. In addition, increasing the number of passes has led to the reduction of wear rate at all the three applied loads. Moreover, for a given sample, increasing the applied load has increased the wear rate, and for a given applied load, with increasing the number of passes, the wear rate decreases. Fig. 9, shows the effect of Ti content on Lancaster wear coefficient at the applied loads of 50, 100, and 150 N. Since the amount of Ti in each layer has been calculated in Table 3, the effect of Ti content on the specific wear rate, also known as Lancaster wear coefficient [38], can be observed. As seen from Fig. 9, at a given applied load, with increasing the amount of Ti from 1 wt% in Fe-B-C-Ti-1 to 2.4 wt% in Fe-B-C-Ti-3, the specific wear rate decreases. Moreover, for a given amount of Ti, the specific wear rate increases with increasing the load. Fig. 10 shows the SEM image taken from the surfaces worn at the applied loads of 100 and 150 N. Some pitting is evident on the worn surfaces of Fe-B-C-Ti-1, Fe-B-C-Ti-2, and Fe-B-C-Ti-3, given in Fig. 10. The adhesive layer on the surface has oxidic nature, confirmed by the EDS analysis of points 1 and 2, shown in Table 6. As can be seen, some layers are about to detach. These layers are crushed due to the continuous contacts between the sliding surfaces and led to the formation of oxide agglomerated particles, finally forming a dense layer between the sliding surfaces. There exists evidence showing the presence and formation of tribological layer. Therefore, the higher the surface hardness of Fe-B-C-Ti-3 is, the longer the oxide layer is supported by the substrate in Fig.10, leading to the less friction coefficient, Fig.7 and less specific wear rate, Fig. 9. Fig. 11 shows the SEM image taken from the wear debris of the samples worn at 100 and 150 N. Two completely different constituents can be seen: (1) fine and coarse agglomerated particles, which their oxidic nature has been confirmed by EDS analysis of points 3 and 4, shown in Table 6, and (2) the tribological layer detached from the surface which is laminar and has been formed by the mixture and compression of the wear debris entrapped between the sliding surfaces, and is composed of iron, oxygen, and titanium according to Table 6. Comparing Figs. 11a, c, and e with Figs. 11b, d and f shows that, with increasing the applied load, the

size of the debris relatively enlarges. The results show that the wear mechanism of the samples worn at lower loads (100 N) is the oxidation wear through the formation and removal of oxidic tribological layer which is consistent with Figs. 7, 10 and 11. This wear mechanism can be explained as follows: at the beginning of sliding, wear debris are produced between the pin and the disk due to surface asperities. These debris are entrapped between the sliding surfaces, and converted to finer particles by crushing and plastic deformation due to their free movement between the sliding surfaces. Then, they are oxidized because of the high temperature induced by frictional heating. After that, the oxidized particles existing in some locations, such as grooves, are agglomerated and formed as a dense oxide layer which is responsible for the reduction of friction coefficient between the sliding surfaces, Fig.7 [39]. The process continues with a competitive mechanism [40]. Oxide layer becomes increasingly thicker and the wear rate decreases. When the thickness of the oxide layer reaches a critical value, it is detached by the fatigue mechanism, occurring after a certain number of contact cycles. Consequently, it becomes a part of wear products, Fig.11.

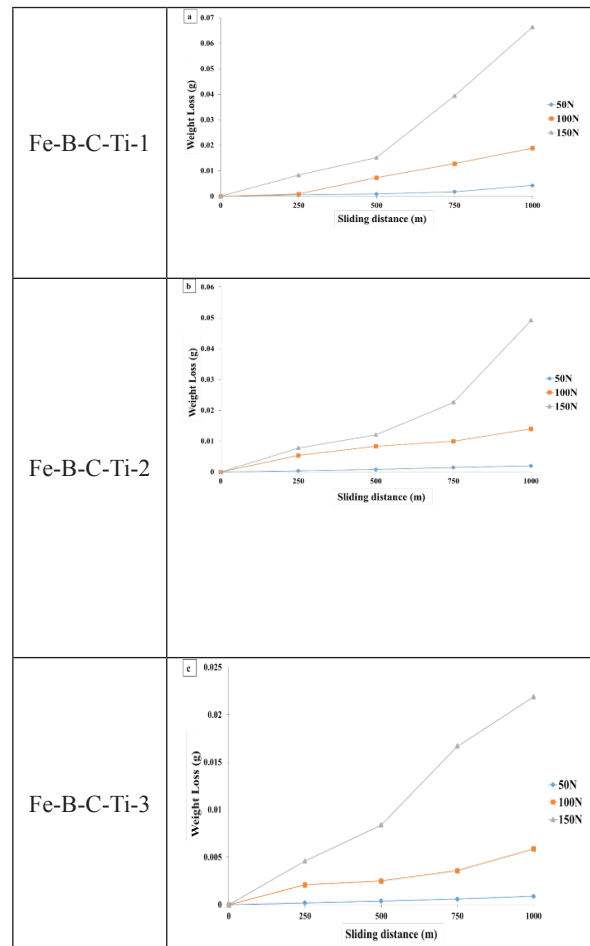


Fig. 6. Weight loss variation during sliding distance for the different testing samples, a) Fe-B-C-Ti-1, b) Fe-B-C-Ti-2, c) Fe-B-C-Ti-3

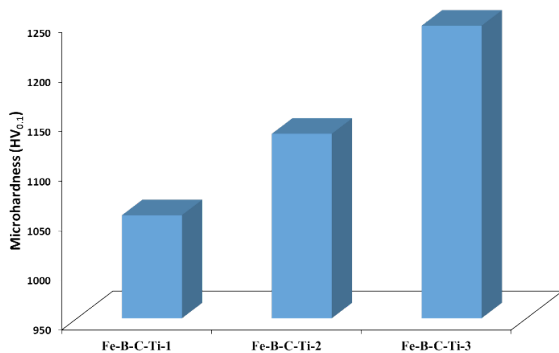


Fig. 5. Microhardness of hardfacing samples

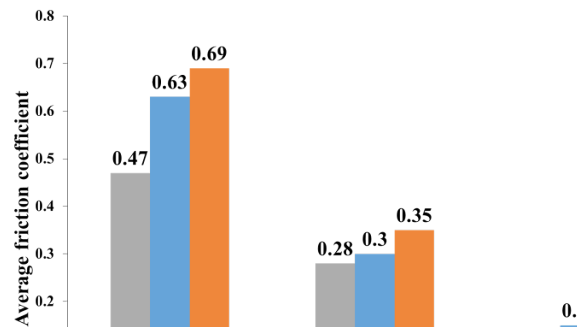


Fig. 7. Variation of average friction coefficient in applied load for different samples.

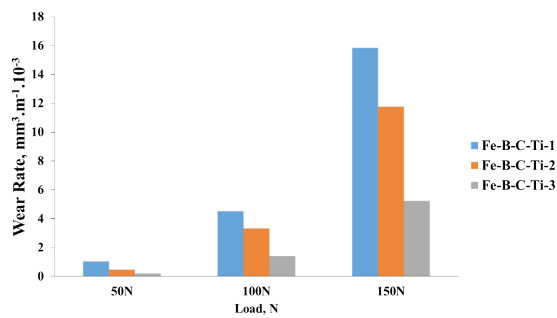


Fig. 8. Variation of wear rate versus applied load for different samples.

The presence of oxygen, titanium, and iron shows that, in addition to oxidation wear, the fine wear debris produced during sliding have been mechanically mixed and then merged with tribological layer. Comparing the images taken from wear debris and tribological layer shows that the laminar particles present in the wear debris have been mainly detached from the tribological layer by the continuous formation and removal of the layer. As the sliding distance increases and the tribological layer becomes thicker, the contact stresses between the sliding surfaces prevent the further growth of the tribological layer after which its destruction rate exceeds its growth rate. Therefore, the tribological layer is crushed and becomes a part of wear products. When the tribological layer

is crushed, its re-formation process begins and the continuous formation and destruction of this layer controls the wear rate. The low wear rate of the samples worn at lower loads, Fig. 8, can be attributed to the competition between the destruction and formation rate of this layer. As seen from Fig. 10, the wear rate is controlled by the destruction and formation rate of this layer. In addition to wear rate reduction, tribological layer hinders the transition to a more severe wear regime and decreases the friction coefficient [38]. After the friction coefficient reduction due to the formation of tribological layer, with the further increase of sliding distance and the destruction of tribological layer, the pin and the disk meet each other and the friction coefficient increases again. Fig. 12 shows the subsurface micrographs of hardfaced samples at the applied load of 150N. Under 150 N, in addition to the presence of tribological layer Fig.10 e, and f, the nucleation and propagation of surface and subsurface cracks occurs Fig. 12. Therefore, it can be concluded that the wear at high load causes severe subsurface deformation due to the high applied stresses [41, 42]. This can lead to the formation of cavities in the subsurface region, providing suitable spots for the crack growth and propagation. After being nucleated and grown, the subsurface cracks are merged together by passing through weak regions (such as the interface of phases) and/or the regions

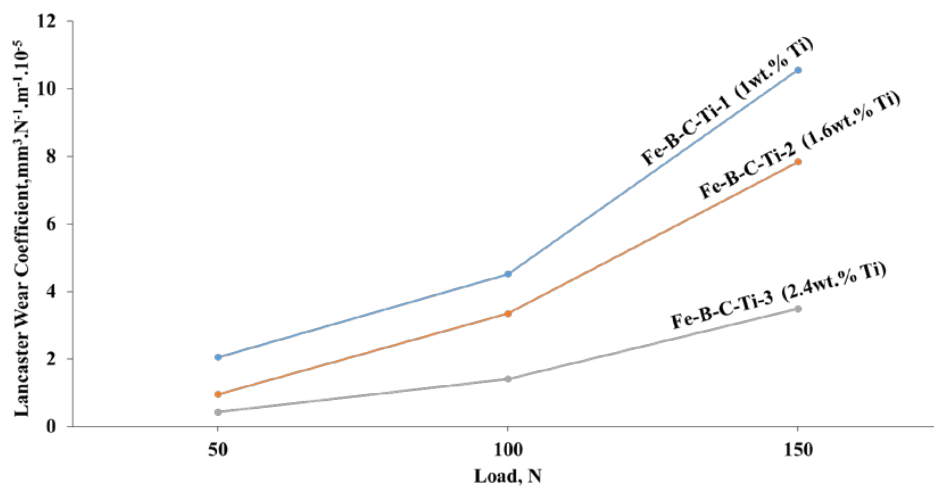


Fig. 9. Lancaster wear coefficient as a function of applied load for titanium contents in different samples.

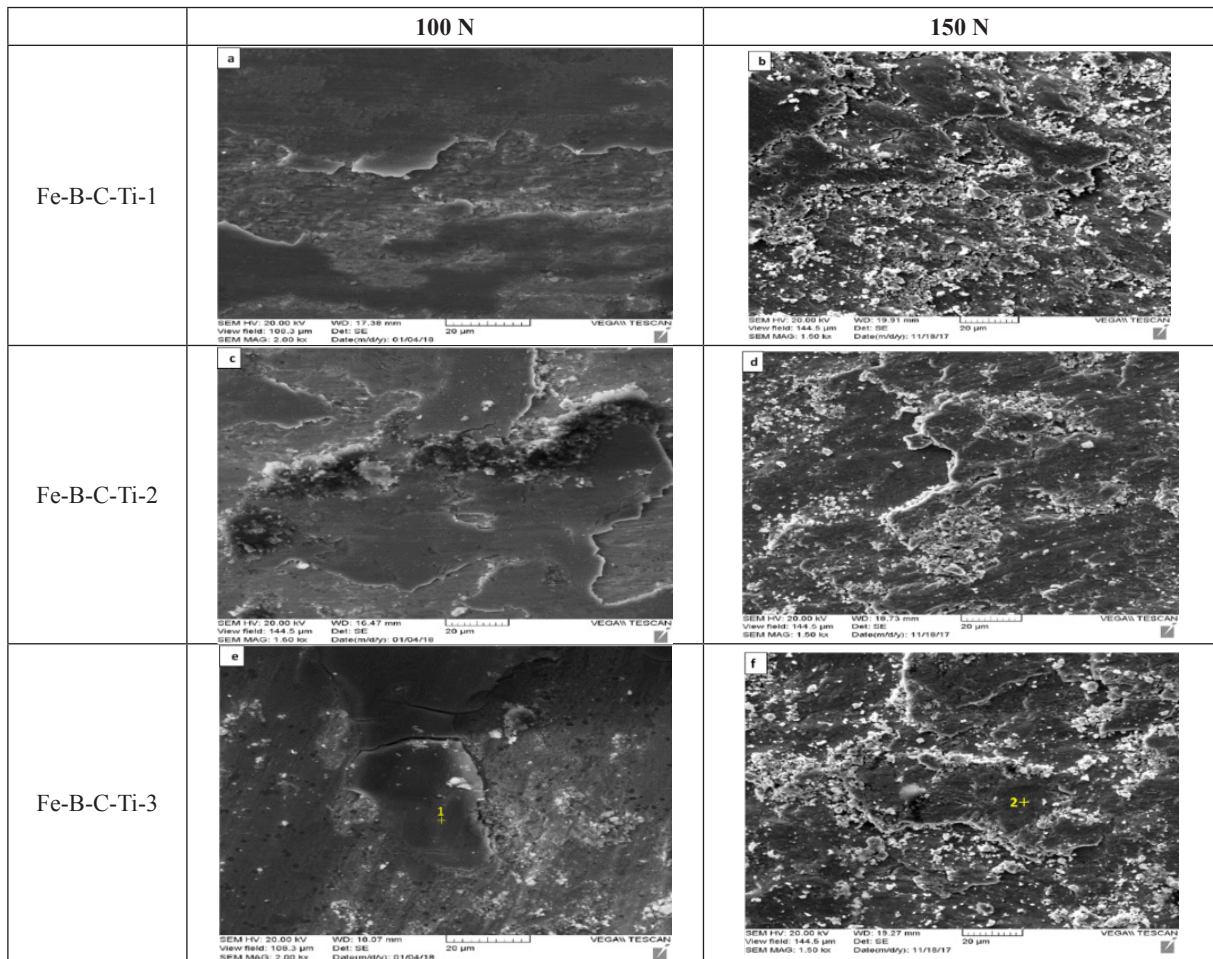
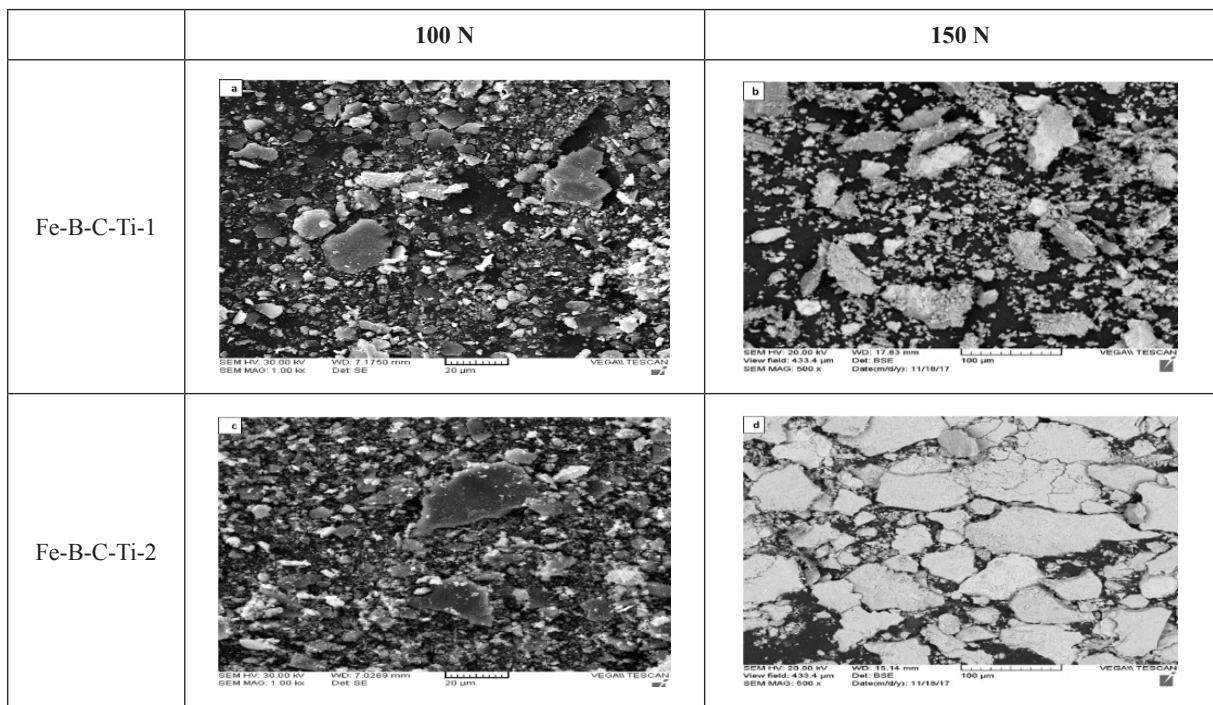


Fig.10. SEM micrographs of worn surfaces for different samples at applied loads.



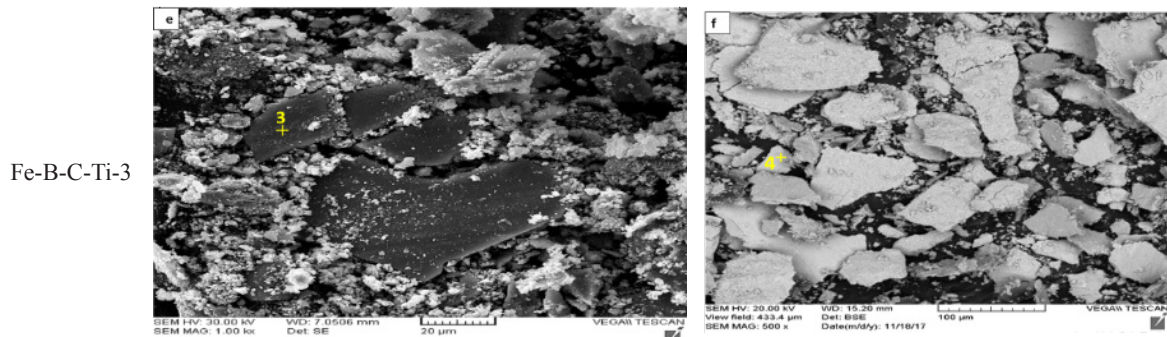


Fig. 11. SEM micrographs of worn debris for different samples at applied loads.

Table.6. EDS results of the marked regions in Fig.10 and Fig.11 (in wt. %).

Phase no.	1	2	3	4
Element				
C	8.99	14.64	8.92	4.18
O	41.87	26.19	51.27	3.17
Ti	1.33	1.05	1.34	1.84
Fe	47.8	58.13	38.46	90.81

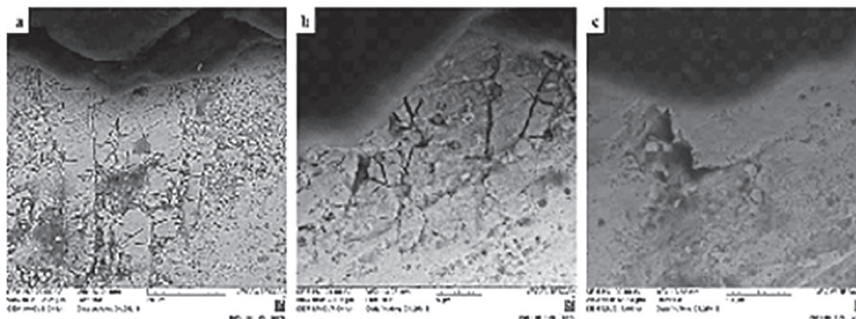


Fig. 12. Longitudinal cross-section of the worn surface of hardfaced samples at the applied load of 150 N, a) Fe-B-C-Ti-1, b) Fe-B-C-Ti-2, c) Fe-B-C-Ti-3

experiencing a severe stress. Then, due to the external stress applied during the wear test, they are detached, leaving the wear zone in the form of lamellar particles [43]. These fragmented metallic particles could be mechanically mixed with the oxides in the contact zone and form a tribolayer (MML) [44] Fig. 12. It should be noted that, according to the images taken from the subsurface Fig. 12 and wear debris Fig. 11, delamination is not the only mechanism present at higher loads (150 N). This can be due to the presence of oxide layers and particles at high loads. In fact, some particles detached by the delamination mechanism are entrapped

between the contact surfaces and become. These entrapped particles become finer as a result of crushing and plastic deformation, and are oxidized because of the high temperature produced by frictional heat. As the wear process continues and the number of oxide particles increases, a thin layer is formed on the surface, reducing the friction between contact surfaces as well as the stress applied on the subsurface region, which in turn, hindering the detachment of particles through delamination. However, after a while, due to the stresses applied during the wear process, this oxide layer is removed from the surface in the form of dense particles.

Subsequently, the stresses applied on the subsurface regions increase, facilitating the detachment of particles through delamination. Therefore, the wear mechanism at high loads is the combination of delamination and oxidation. However, the delamination is the main and dominant mechanism. The delamination of surface layers does not mean the oxidation wear is fully absent. In fact, during the wear process, both layer delamination and oxide debris are present, and the formation and destruction of the oxide layer is an ongoing process. But, the destruction rate of the oxide layer and its critical thickness are the differences between delamination and mild wear mechanism.

4. CONCLUSIONS

The aim of this work was to study of microstructure, hardness, and dry sliding wear of hardfaced layers produced by FCAW using cored wire Fe-B-C-Ti alloy.

The results can be summarized as follows;

1. With increasing Ti content from 1wt% in sample Fe-B-C-Ti-1 to 2.4wt.% in sample Fe-B-C-Ti-3, the microstructure changed from TiC + layered eutectic α -Fe₂B to primary Fe₂B + TiC + TiB₂ + vermicular eutectic α -Fe₂₃(B,C)₆
2. With increasing boron content, no detrimental FeB phase and cracks formed around Fe₂B.
3. At applied loads, Fe-B-C-Ti-3 and Fe-B-C-Ti-1 have the lowest and highest wear rate, respectively. The higher wear resistance of Fe-B-C-Ti-3 is related to the higher levels of B and Ti, which has increased hardness.
4. Wear mechanism of the samples worn at lower loads (50, and 100 N) is the oxidation wear through the formation and removal of oxidic tribological layer.
5. The dominant mechanism under 150 N is delamination along with oxidation.

REFERENCES

1. Kováč, I., Mikuš, R., Žarnovský, J., Drlička, R., Žitňanský, J. and Výrostková, A., "Creation of wear resistant boride layers on selected

- steel grades in electric arc remelting process". *Kovove Mater.*, 2014, 52, 387–394.
2. Gou, J., Wang, Y., Sun, J. and Li, X., "Study of work function and dry sliding wear behavior of Fe-based hardfacing alloys with and without nano rare earth oxides". *J. Alloys Compd.*, 2017, 713, 255-265.
3. Gou, J., Lu, P., Wang, Y., Liu, S. and Zou, Z., "Effect of nano-additives on microstructure, mechanical properties and wear behaviour of Fe–Cr–B hardfacing alloy". *Appl. Surf. Sci.*, 2016, 360, 849-857.
4. Kim, J. H., Ko, K. H., Noh, S. D., Kim, G. G. and Kim, S. J., "The effect of boron on the abrasive wear behavior of austenitic Fe-based hardfacing alloys". *Wear*, 2009, 267, 1415-1419.
5. Rovatti, L., Lemke, J. N., Emami, A., Stejskal, O., and Vedani, M., "Effects of V Addition on Microstructure and Hardness of Fe-C-B-Ni-V Hardfacing Alloys Cast on Steel Substrates". *J. Mater. Eng. Perform.*, 2015, 24, 4755–4763.
6. Gunther, K., Bergmann, J. P. and Suchodoll, D., "Hot wire-assisted gas metal arc welding of hypereutectic FeCrC hardfacing alloys: Microstructure and wear properties". *Surf. Coat. Technol.*, 2018, 334, 420-428.
7. Correa, E. O., Alcântara, N. G., Valeriano, L. C., Barbedo, N. D. and Chaves, R. R., "The effect of microstructure on abrasive wear of a Fe–Cr–C–Nb hardfacing alloy deposited by the open arc welding process". *Surf. Coat. Technol.*, 2015, 276, 479–484.
8. Yuksel, N., and Sahin, S., "Wear behavior–hardness–microstructure relation of Fe–Cr–C and Fe–Cr–C–B based hardfacing alloys". *Mater. Des.*, 2014, 58, 491–498.
9. Gualco, A., Svoboda, H. G. and Surian, E. S., "Study of abrasive wear resistance of Fe-based nanostructured hardfacing". *Wear*, 2016, 360-361, 14-20.
10. Amushahi, M. H., Ashrafizadeh, F. and Shamanian, M., "Characterization of boride-rich hardfacing on carbon steel by arc spray and GMAW processes". *Surf. Coat. Technol.*, 2010, 204, 2723–2728.
11. Manna, I., Majumdar, J. D., Chandra, B. R., Nayak, S. and Dahotre, N. B., "Laser surface cladding of Fe–B–C, Fe–B–Si and Fe–B–C–Si–Al–C on plain carbon steel". *Surf. Coat.*

- Technol., 2006, 201, 434-440.
12. Xibao, W., Xiaofeng, W. and Zhongquan, S., "The composite Fe-Ti-B-C Coatings by PTA powder surfacing process. Surf". Coat. Technol., 2005, 192, 257-262.
 13. Zahiri, R., Sundaramoorthy, R., Lysz, P. and Subramanian, C., "Hardfacing using ferro-alloy powder mixtures by submerged arc welding". Surf. Coat. Technol., 2014, 260, 220-229.
 14. Coronado, J. J., Caicedo, H. F. and Gomez, A. L., "The effects of welding processes on abrasive wear resistance for hard-facing deposits". Trib Int., 2009, 42, 745-749.
 15. Yıldızlı, K., Eroglu, M., and Karamış, M. B., "Microstructure and erosive wear behavior of weld deposits of high manganese electrode". Surf. Coat. Technol., 2007, 201, 7166-7173.
 16. Lemke, J. N., Rovatti, L., Colombo, M. and Vedani, M., "Interrelation between macroscopic, microscopic and chemical dilution in hardfacing alloys". Mater. Des., 2016, 91, 368-377.
 17. Yang, K., Gao, Y., Yang, K., Bao, Y. and Jiang, Y., "Microstructure and wear resistance of Fe-Cr13-C-Nb hardfacing alloy with Ti addition". Wear, 2017, 376-377, 1091-1096.
 18. Gualco, A., Svoboda, H. G., Surian, E. S., "Effect of welding parameters on microstructure of Fe-based nanostructured weld overlay deposited through FCAW-S". Weld Int., 2016, 19, 255-263.
 19. Sabet, H., Khierandish, Sh., Mirdamadi, S. and Goodarzi, M., "The Microstructure and Abrasive Wear Resistance of Fe-Cr-C Hardfacing Alloys with the Composition of Hypoeutectic, Eutectic, and Hypereutectic at Cr/C=6", Tribol Lett, 2011, 44, 237-245.
 20. Zhuang, M., Li, M., Wang, J., Ma, Z. and Yuan, S., "Study on Composition, Microstructure and Wear Behavior of Fe-B-C Wear-Resistant Surfacing Alloys". J. Mater. Eng. Perform., 2017, 26, 6182-6192.
 21. Yi, D., Xing, J., Fu, H., Zhang, Z., Chen, J., Zhang, J., Peng, J. and Shi, Y., "Effect of Fe₂B boride orientation on abrasion wear resistance of Fe-B cast alloy". China Foundry, 2017, 14, 145-151.
 22. Zhang, J., Gao, Y., Xing, J., Ma, S., Yi, D. and Yan, J., "Effects of Chromium Addition on Microstructure and Abrasion Resistance of Fe-B Cast Alloy". Tribol Lett, 2011, 44, 31-39.
 23. Jian, Y., Huang, Z., Xing, J. and Wang, B., "Effects of chromium addition on fracture toughness and hardness of oriented bulk Fe₂B crystals". Mater. Charact., 2015, 110, 138-144.
 24. Yu, L. G., Chen, X. J., Khor, K. A. and Sundararajan, G., "FeB/Fe₂B phase transformation during SPS pack-boriding: Boride layer growth kinetics". Acta Mater., 2005, 53, 2361-2368.
 25. Eroglu, M., "Boride coatings on steel using shielded metal arc welding electrode: Microstructure and hardness". Surf. Coat. Technol., 2009, 203, 2229-2235.
 26. Jian, Y., Huang, Z., Xing, J., Zheng, B., Sun, L., Liu, Y. and Liu, Y., "Effect of improving Fe₂B toughness by chromium addition on the two-body abrasive wear behavior of Fe-3.0 wt% B cast alloy". TRIBOL INT, 2016, 101, 331-339.
 27. Motallebzadeh, A., Dilektasli, E., Baydogan, M., Atar, E. and Cimenoglu, H., "Evaluation of the effect of boride layer structure on the high temperature wear behavior of borided steels", Wear, 2015, 328-329, 110-114.
 28. Huang, Z., Xing, J. and Guo, C., "Improving fracture toughness and hardness of Fe₂B in high boron white cast iron by chromium addition". Mater. Des., 2010, 31, 3084-3089.
 29. Yi, D., Xing, J., Zhang, Z., Fu, H. and Yang, C., "Effect of Titanium and Nitrogen Additions on the Microstructures and Three-Body Abrasive Wear Behaviors of Fe-B Cast Alloys". Tribol Lett, 2014, 54, 107-117.
 30. Singla, Y. K., Arora, N. and Dwivedi, D. K., "Dry sliding adhesive wear characteristics of Fe-based hardfacing alloys with different CeO₂ additives - A statistical analysis". TRIBOL INT, 2017, 105, 229-240.
 31. Dawei, Y., Jiandong, X., Hanguang, F., Shengqiang, M. and Zhuxin, L., "Effect of Rare Earth-Al Additions on the Structural Variations of Medium Carbon Fe-B Cast Alloy". Key Eng. Mater., 2011, 457, 213-218.
 32. Huang, Z., Xing, J. and Lv, L., "Effect of tungsten addition on the toughness and hardness of Fe₂B in wear-resistant Fe-B-C cast alloy". Mater. Charact., 2013, 75, 63-68.
 33. Hsieh, C. C., Liu, Y. C., Wang, J. S. and Wu, W., "Microstructural Evolution with Various Ti

- Contents in Fe-Based Hardfacing Alloys Using a GTAW Technique”. *Met. Mater. Int.*, 2014, 20, 701-712.
34. Liu, Y., Li, B., Li, J., He, L., Gao, S. and Nieh, T. G., “Effect of titanium on the ductilization of Fe-B alloys with high boron content”. *Mater. Lett.*, 2010, 64, 1299-1301.
 35. Colaço, F. H. G. and Maranhão, O., “Evaluation of mass loss of weld-deposited hardfacing with cored wire Ti-FeCrC alloy”. *Weld Int.*, 2016, 30, 283-292.
 36. Lai, H. H., Hsieh, C. C., Lin, C. M. and Wu, W., “Effect of oscillating traverse welding on microstructure evolution and characteristic of hypoeutectic hardfacing alloy”. *Surf. Coat. Technol.*, 2014, 239, 233-239.
 37. Duschanek, H. and Rogl, P., “A Critical Assessment and Thermodynamic Calculation of the Boron-Carbon-Titanium (B -C-Ti) Ternary System”. *J Phase Equilib*, 1995, 16, 46-60.
 38. Lancaster, J. K., “Dry bearings: a survey of materials and factors affecting their performance”. *TRIBOL INT*, 1973, 6, 219-251.
 39. DaConceição, L. and D’Oliveira, A. S., “The effect of oxidation on the tribolayer and sliding wear of a Co-based coating”. *Surf. Coat. Technol.*, 2016, 288, 69-78.
 40. KumarSingla, Y., Arora, N. and Dwivedi, D. K., “Dry sliding adhesive wear characteristics of Fe-based hardfacing alloys with different CeO₂ additives – A statistical analysis”. *TRIBOL INT*, 2017, 105, 229-240.
 41. Stachowiak, G. W. and Batchelor, A. W., “Engineering Tribology. Butterworth Heinemann”, 4th Ed., USA, 2013.
 42. Bhushan, B., “Modern tribology handbook”. CRC Press, USA, 2001.
 43. Suh, N. P., “The delamination theory of wear”. *Wear*, 1973, 25, 111-124.
 44. Abouei, V., Saghafian, H. and Kheirandish, Sh., “An investigation of the wear behaviour of 0.2% C dual phase steels”. *J Mater Process Tech*, 2008, 203, 107-112.